

*Annual Review of Condensed Matter Physics*  
Evolution from Bardeen–  
Cooper–Schrieffer to  
Bose–Einstein Condensation in  
Two Dimensions: Crossovers  
and Topological Quantum  
Phase Transitions

C.A.R. Sá de Melo and Senne Van Loon

School of Physics, Georgia Institute of Technology, Atlanta, Georgia, USA;  
email: carlos.sademelo@physics.gatech.edu

Annu. Rev. Condens. Matter Phys. 2024. 15:109–29

The *Annual Review of Condensed Matter Physics* is online at [conmatphys.annualreviews.org](https://conmatphys.annualreviews.org)

<https://doi.org/10.1146/annurev-conmatphys-032922-115341>

Copyright © 2024 by the author(s). This work is licensed under a Creative Commons Attribution 4.0 International License, which permits unrestricted use, distribution, and reproduction in any medium, provided the original author and source are credited. See credit lines of images or other third-party material in this article for license information.

ANNUAL  
REVIEWS **CONNECT**

[www.annualreviews.org](https://www.annualreviews.org)

- Download figures
- Navigate cited references
- Keyword search
- Explore related articles
- Share via email or social media

### Keywords

BCS, BEC, crossover, phase transitions, 2D, quantum phases, topology

### Abstract

We review aspects of the evolution from Bardeen–Cooper–Schrieffer (BCS) to Bose–Einstein condensation (BEC) in two dimensions, which have now become relevant in systems with low densities, such as gated superconductors  $\text{Li}_x\text{ZrNCl}$ , magic-angle twisted trilayer graphene, FeSe,  $\text{FeSe}_{1-x}\text{S}_x$ , and ultracold Fermi superfluids. We emphasize the important role played by chemical potentials in determining crossovers or topological quantum phase transitions during the BCS–BEC evolution in one-band and two-band superfluids and superconductors. We highlight that crossovers from BCS to BEC occur for pairing in nonnodal  $s$ -wave channels, whereas topological quantum phase transitions, in which the order parameter symmetry does not change, arise for pairing in any nodal higher angular momentum channels, such as  $d$ -wave. We conclude by discussing a few open questions regarding the BCS-to-BEC evolution in 2D, including modulus fluctuations of the order parameter, tighter upper bounds on critical temperatures, and the exploration of lattice effects in two-band superconductors and superfluids.

## 1. INTRODUCTION

There has been an explosion of experimental work addressing the evolution from Bardeen–Cooper–Schrieffer (BCS) to Bose–Einstein condensation (BEC) in two dimensions (2D), as a function of carrier density in condensed matter (1–9) and as a function of interaction strength in ultracold Fermi superfluids (10, 11). To understand the importance of these experimental developments and their connection to theoretical efforts, we review below some aspects of superconductivity and superfluidity.

The first successful microscopic theory of superconductivity was proposed by Bardeen, Cooper & Schrieffer (12) in 1957, and it was based on the idea of pairing electrons of opposite spin in momentum space. BCS proposed a variational many-body wave function with pairing correlations that was able to explain weakly interacting and sufficiently high density  $s$ -wave superconductors in three dimensions (3D). Earlier, in 1957, a competing theory was proposed by Schafroth, Butler & Blatt (SBB) (13), based on the idea that correlated tightly bound pairs of electrons could become superconducting via BEC of these molecular pairs. SBB suggested a mechanism similar to what happens in  $^4\text{He}$ , where BEC provides a condensate fraction and interactions between bosons ensure their superfluidity.

As discussed in John Markus Blatt’s book, *Theory of Superconductivity* (14), Max Schafroth proposed an antisymmetrized real space wave function involving products of two-electron states to describe real space pairs of electrons in 3D. Even though the SBB theory was published slightly earlier, fate would favor the BCS theory because of its remarkable success in explaining the experimental results of the time. In the BCS paper (12), it was clearly emphasized that their pairing theory did not lead to BEC! This was described in their famous quote (12, p. 1177):

Our picture differs from that of Schafroth, Butler, and Blatt, *Helv. Phys. Acta* 30, 93 (1957), who suggest that pseudomolecules of pairs of electrons of opposite spin are formed. They show if the size of the pseudomolecules is less than the average distance between them, and if other conditions are fulfilled, the system has properties similar to that of a charged Bose–Einstein gas, including a Meissner effect and a critical temperature of condensation. Our pairs are not localized in this sense, and our transition is not analogous to a Bose–Einstein condensation.

Surprisingly, it took several years to realize that Schafroth’s and BCS’s wave functions were the opposite limits of the same theory: in one, pairing occurs in real space, and in the other, it occurs in momentum space. This was first recognized by Leggett (15, 16), who used Schafroth’s wave function to describe the connection between the BEC and BCS regimes at zero temperature ( $T = 0$ ) as interaction strength is changed for a system with fixed particle density in 3D. Leggett’s work was generalized to finite temperatures by Nozières & Schmitt-Rink (NSR) (17) using a diagrammatic approach. A few years later, Sá de Melo and colleagues (18, 19) developed a functional integral approach that recovers both Leggett’s and NSR results while providing insights into the fluctuations around the critical temperature, the nature of the collective modes, and the fundamental difference between the correlation length and the pair size associated with Cooper pairing. For several more years, these theoretical developments were merely of academic interest, because there were no experiments that could change either the interactions from weak to strong at fixed particle density or the particle density from low to high at fixed interaction strength. Therefore, the BCS to BEC evolution remained unexplored experimentally until the early 2000s.

With the ability to trap and cool Fermi atoms, such as  $^6\text{Li}$  (20–25) and  $^{40}\text{K}$  (26, 27), to very low temperatures, it was found that Feshbach–Fano (28, 29) resonances existed in both types of atoms. This opened the door for tuning  $^6\text{Li}$ – $^6\text{Li}$  or  $^{40}\text{K}$ – $^{40}\text{K}$  interactions at fixed density with the help of external magnetic fields. Both  $s$ - and  $p$ -wave interactions were tunable in these two

## EVOLUTION FROM BCS TO BEC OR FROM BCS TO BOSE SUPERFLUIDITY AND SUPERCONDUCTIVITY?

Although the terminology *evolution from BCS to BEC* is accurate in 3D, it is not strictly correct in 2D because there is no BEC in dimensions lower than three. Thus, a more appropriate nomenclature in 2D is *evolution from BCS to Bose superfluidity or superconductivity*. However, we use the language *BCS to BEC* throughout the review for the mere convenience of having a single jargon applied to three-dimensional or two-dimensional superfluids and superconductors. The terminology also seems to be preferred in the existing literature and should facilitate online searches about this evolution in 3D and 2D.

systems. However, most of the experimental work that followed investigated *s*-wave systems, because the lifetime of paired fermions in this channel was sufficiently long to detect superfluidity (20, 23, 24, 26). Unfortunately, the corresponding lifetime in the *p*-wave channel was much shorter than the timescale required to observe superfluidity (30, 31). After an initial exploration of three-dimensional superfluids in harmonic traps, theoretical and experimental efforts expanded to include two-dimensional systems, either by tight harmonic confinement along one direction (32–35) or by creating highly anisotropic optical lattices (36–40). Until recently, all cold-atom experiments exhibited some degree of inhomogeneity caused by the harmonic confinement or the harmonic envelope of optical lattices. Therefore, theorists had to rely on the local density approximation to make direct comparison to experiments, often leading to unreliable findings (41, 42). Fortunately, with the development of high-quality digital mirror devices, the creation of homogeneous three- and two-dimensional optical box potentials was recently made possible (43–47). This tremendously facilitates comparisons to theoretical work in the continuum and in uniform optical lattices (34, 48–50). (See the sidebar titled Evolution from BCS to BEC or from BCS to Bose Superfluidity and Superconductivity.)

The use of optical box potentials to trap ultracold fermions has allowed for the exploration of homogeneous two-dimensional superfluids from the BCS to BEC regime, where particle density is fixed, but interactions are changed (44, 51). This effort now also has a parallel in two-dimensional superconductors, where gating and doping techniques have permitted the investigation of two-dimensional superconductors from the BCS to BEC regime, where the interactions are fixed, but carrier densities are changed. In particular, two-dimensional materials such as Lithium-doped nitrides ( $\text{Li}_x\text{ZrNCl}$ ) (1, 2), magic-angle twisted trilayer graphene (3–5), FeSe (6, 7), and  $\text{FeSe}_{1-x}\text{S}_x$  (8, 9), are now considered prime candidates to study BCS–BEC crossovers and quantum phase transitions.

In this review, we discuss fundamental concepts involving the evolution from BCS to BEC superfluidity and superconductivity in 2D, emphasizing the role of chemical potentials in describing crossovers and quantum phase transitions. We analyze the cases of one-band and two-band systems with *s*-wave or higher angular momentum pairing (e.g., *d*-wave) and emphasize that the BCS–BEC evolution is a crossover for nonnodal *s*-wave systems but exhibits topological quantum phase transitions for nodal higher wave pairing. Whenever applicable, connections and comparisons are made to experiments in ultracold atomic superfluids and condensed matter superconductors.

The remainder of this review is organized as follows. In Section 2, we discuss the fundamental role that the chemical potential plays in the evolution from BCS to BEC in 3D and 2D, with initial focus on one-band superfluids and superconductors. In Section 3, we analyze the BCS–BEC crossover in two-dimensional homogeneous *s*-wave systems covering ultracold Fermi superfluids and condensed matter superconductors. In Section 4, we consider higher angular

momentum (e.g.,  $d$ -wave) pairing with nodal structures and identify the existence of topological quantum phase transitions as the chemical potential crosses a critical value in 2D. In the following sections, we generalize these concepts to two-band systems. In Section 5, we discuss the role played by chemical potentials in two-band superfluids and superconductors. In Section 6, we explain the BCS–BEC crossover in two-band systems and make connections to FeSe, FeSe<sub>1-x</sub>S<sub>x</sub>, and Li<sub>x</sub>ZrNCl. In Section 7, we examine the existence of topological quantum phase transitions for higher angular momentum pairing as chemical potentials are changed by either fixing interactions and changing density or fixing density and changing interactions. A possible connection to magic-angle twisted trilayer graphene is discussed. In Section 8, we summarize the main points of the review, and in Section 9, we briefly discuss a few open questions and provide an outlook for further investigations.

## 2. THE FUNDAMENTAL ROLE OF THE CHEMICAL POTENTIAL

Irrespective of dimensionality, and whether a crossover or a quantum phase transition occurs, the chemical potential  $\mu$  plays a fundamental role in the evolution from the BCS to the BEC regime in superconductors and superfluids (52, 53). In one-band systems, the quasiparticle energy spectrum of singlet superconductors and superfluids is quite generally

$$E_{\mathbf{k}} = \sqrt{\xi_{\mathbf{k}}^2 + |\Delta_{\mathbf{k}}|^2} \quad 1.$$

in any theory that invokes pairing. Here,  $\mathbf{k}$  is the momentum;  $\xi_{\mathbf{k}} = \epsilon_{\mathbf{k}} - \mu$  is the independent particle energy  $\epsilon_{\mathbf{k}}$  with respect to the chemical potential  $\mu$ ; and  $\Delta_{\mathbf{k}} = |\Delta|\Gamma_{\mathbf{k}}$  is the order parameter, where  $\Gamma_{\mathbf{k}}$  contains the pairing symmetry and interaction range. Within pairing theories, the discussion below is universal, provided that  $|\Delta| \neq 0$  and that no competing phases have lower free energy than the superfluid or superconducting state.

Without specifying density or interactions, consider first the parabolic dispersion  $\epsilon_{\mathbf{k}} = \hbar^2 \mathbf{k}^2 / 2m$ , where  $m$  is the mass of the fermion. When  $\Delta_{\mathbf{k}}$  is characterized by a single angular momentum channel  $\ell \neq 0$  and time-reversal symmetry is not broken, it is guaranteed that  $\Delta_{\mathbf{k}}$  has nodes along specific directions, defined by the angular momentum quantum numbers  $\ell$  and  $m$  in 3D and by  $\ell$  in 2D. For singlet pairing, the order parameters can be  $\Delta_{\mathbf{k}} = |\Delta|\gamma_{|\mathbf{k}|}^{3D} F_{\ell m}(\theta, \phi)$  in 3D or  $\Delta_{\mathbf{k}} = |\Delta|\gamma_{|\mathbf{k}|}^{2D} G_{\ell}(\phi)$  in 2D. Here, the function  $F_{\ell m}(\theta, \phi)$  is  $Y_{00}(\theta, \phi) = 1/\sqrt{4\pi}$  for  $s$ -wave ( $\ell = 0$ ), and  $d_{3z^2-r^2}$ ,  $d_{x^2-y^2}$ ,  $d_{xy}$ ,  $d_{yz}$ , or  $d_{xz}$  for  $d$ -wave ( $\ell = 2$ ), whereas  $G_{\ell}(\phi) = 1$  for  $s$ -wave and  $G_{\ell}(\phi) = \cos 2\phi$  for  $d$ -wave. The functions  $\gamma_{|\mathbf{k}|}^{3D}$  and  $\gamma_{|\mathbf{k}|}^{2D}$  depend only on the modulus  $|\mathbf{k}|$  and contain information about the interaction range.

When the chemical potential  $\mu$  lies above the bottom of the band  $\epsilon_{\mathbf{k}}$ , that is,  $\mu > 0$ , there is a set of momenta (loci)  $\mathbf{k}_{\mu}$  where  $\xi_{\mathbf{k}_{\mu}} = 0$ , leading to  $\hbar|\mathbf{k}_{\mu}| = \sqrt{2m\mu}$ . In this case,  $\min[E_{\mathbf{k}}] = |\Delta_{\mathbf{k}_{\mu}}|$ , meaning that if the order parameter is nodeless (e.g.,  $s$ -wave), then there is a gap in  $E_{\mathbf{k}}$  at  $\mathbf{k}_{\mu}$ . However, if the order parameter has nodes (e.g.,  $d$ -wave), then  $E_{\mathbf{k}}$  is gapless, which is a characteristic of all nodal order parameters for  $\ell \neq 0$ . In contrast, when  $\mu$  lies below the bottom of the band  $\epsilon_{\mathbf{k}}$ , that is,  $\mu < 0$ , there are no momentum loci where  $\xi_{\mathbf{k}} = 0$ , thus  $\min[\xi_{\mathbf{k}}] = |\mu|$  occurs at  $\mathbf{k} = \mathbf{0}$  and  $\min[E_{\mathbf{k}}] = \sqrt{\mu^2 + |\Delta_{\mathbf{k}=\mathbf{0}}|^2}$ . In this situation, there is always a full gap in  $E_{\mathbf{k}}$  for order parameters without nodes (e.g.,  $s$ -wave) or with nodes (e.g.,  $d$ -wave). Either in 2D or 3D,  $\gamma_{|\mathbf{k}|} \sim |\mathbf{k}|^{\ell}$  vanishes as  $|\mathbf{k}| \rightarrow 0$  for  $\ell \neq 0$ , in which case  $\min[E_{\mathbf{k}}] = |\mu|$  depends solely on  $\mu$ . For  $\ell = 0$ , the qualitative change in  $E_{\mathbf{k}}$  from indirectly gapped at  $\mathbf{k}_{\mu}$ , when  $\mu > 0$ , to directly gapped at  $\mathbf{k} = \mathbf{0}$ , when  $\mu < 0$ , is a key point in understanding the crossover from BCS to BEC. For  $\ell \neq 0$ , correspondingly, the qualitative change in  $E_{\mathbf{k}}$  from gapless at  $\mathbf{k}_{\mu}$ , when  $\mu > 0$ , to directly gapped at  $\mathbf{k} = \mathbf{0}$ , when  $\mu < 0$ , is fundamental in identifying a quantum phase transition in the evolution from BCS to BEC. In **Figure 1**, schematic plots reveal the qualitative difference

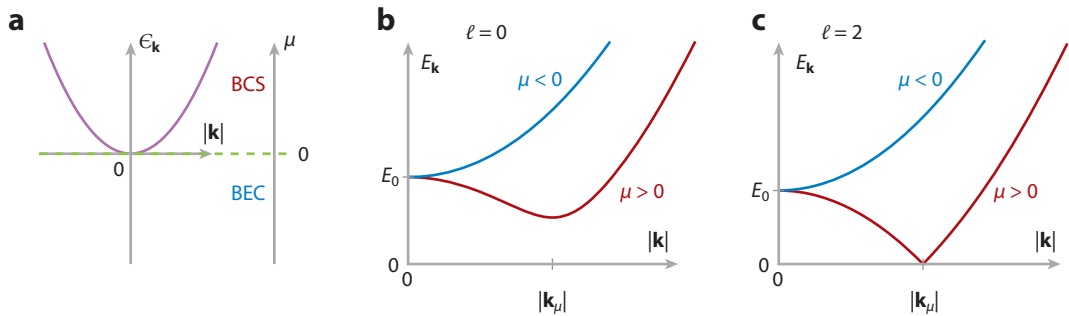


**Figure 1**

(a) Phase diagram showing the BCS ( $\mu > 0$ ) and BEC ( $\mu < 0$ ) regions for a continuum particle-like parabolic dispersion  $\epsilon_{\mathbf{k}} = \hbar^2 \mathbf{k}^2 / 2m$ . For nodal order parameters, the point  $\mu = 0$  indicates a quantum phase transition. (b) The crossover from BCS ( $\mu > 0$ ) to BEC ( $\mu < 0$ ) for  $\ell = 0$  (*s*-wave), where  $E_{\mathbf{k}}$  is always gapped. (c) The quantum phase transition from BCS ( $\mu > 0$ ) to BEC ( $\mu < 0$ ) for  $\ell = 2$  (*d*-wave), where  $E_{\mathbf{k}}$  changes from gapless to gapped. Abbreviations: BCS, Bardeen–Cooper–Schrieffer; BEC, Bose–Einstein condensation.

between  $\ell = 0$  and  $\ell = 2$ . In **Figure 1a**, the phase diagram indicating the BCS and BEC regions as  $\mu$  changes from positive to negative is shown. The quasiparticle energy  $E_{\mathbf{k}}$  for  $\ell = 0$  is drawn in **Figure 1b**, where a crossover occurs (15). The behavior of  $E_{\mathbf{k}}$  for  $\ell = 2$  is plotted in **Figure 1c**, where a quantum phase transition emerges (53–55). This quantum phase transition occurs without changing the symmetry of the order parameter, and thus cannot be understood in the Landau framework of symmetry-based phase transitions, but rather has a topological nature that produces thermodynamic signatures of a second- or higher-order phase transition according to the Ehrenfest classification (53).

There is another fundamental difference between  $\ell = 0$  and  $\ell \neq 0$  pairing in 2D, with respect to the existence of two-body bound states. For *s*-wave, there is always a two-body bound state for arbitrarily small interactions, meaning that the crossover line  $\mu = 0$ , in the density versus interaction plane, can always be traversed by either fixing interactions and changing density or vice-versa (53, 56). However, for *d*-wave, there is a critical interaction for the emergence of two-body bound states, meaning that the quantum phase transition line  $\mu = 0$  can always be crossed by fixing density and changing interactions, but not necessarily by fixing interactions and changing density (53, 56)

A similar situation also arises in lattices, where the independent particle dispersion  $\epsilon_{\mathbf{k}}$  is no longer parabolic. Let us mention two simple examples. A single uncorrelated tight-binding band may have  $\epsilon_{\mathbf{k}} = -2t \sum_i \cos k_i a$ , where  $i \in \{x, y\}$  in 2D (square lattice) or  $i \in \{x, y, z\}$  in 3D (cubic lattice). A single correlated tight-binding band may have  $\epsilon_{\mathbf{k}} = -2t \sum_i \cos k_i a + \epsilon_{\mathbf{k}}^{(\text{co})}$ , where  $\epsilon_{\mathbf{k}}^{(\text{co})}$  are due to correlations emerging from Hartree–Fock theories, for example. Provided that the uncorrelated or correlated bands are parity even and have particle–hole symmetry with respect to  $\epsilon_c = (\max[\epsilon_{\mathbf{k}}] - \min[\epsilon_{\mathbf{k}}]) / 2$ , a few general statements can be made with respect to the quasiparticle excitation spectrum  $E_{\mathbf{k}}$ , displayed in Equation 1. For  $\min[\epsilon_{\mathbf{k}}] \leq \mu \leq \max[\epsilon_{\mathbf{k}}]$ , there are always loci  $\mathbf{k}_{\mu}$  in momentum space where  $\xi_{\mathbf{k}_{\mu}} = 0$ , which requires  $\epsilon_{\mathbf{k}_{\mu}} = \mu$ . If the order parameter is nodeless, then  $\min[E_{\mathbf{k}}] = |\Delta_{\mathbf{k}_{\mu}}|$  corresponds to a gap in  $E_{\mathbf{k}}$ . However, if the order parameter has nodes, then  $\min[E_{\mathbf{k}}] = 0$  along the nodal directions of the order parameter. In contrast, for  $\mu \leq \min[\epsilon_{\mathbf{k}}]$  or  $\mu \geq \max[\epsilon_{\mathbf{k}}]$ , there are no loci in momentum space where  $\xi_{\mathbf{k}} = 0$ , leading to  $\min[E_{\mathbf{k}}] = \sqrt{(\min[\epsilon_{\mathbf{k}}] - \mu)^2 + |\Delta_{\mathbf{k}_{\min}}|^2}$  when  $\mu \leq \min[\epsilon_{\mathbf{k}}]$  or to  $\min[E_{\mathbf{k}}] = \sqrt{(\max[\epsilon_{\mathbf{k}}] - \mu)^2 + |\Delta_{\mathbf{k}_{\max}}|^2}$  when  $\mu \geq \max[\epsilon_{\mathbf{k}}]$ . In simple cases of particle-like  $\epsilon_{\mathbf{k}}$ , the values of  $\min[\epsilon_{\mathbf{k}}]$  occur at  $\mathbf{k} = \mathbf{0}$ , and the values of  $\max[\epsilon_{\mathbf{k}}]$  occur at the Brillouin zone boundaries. The situation is reversed for hole-like  $\epsilon_{\mathbf{k}}$ . In **Figure 2**, we use the qualitative behavior of  $\epsilon_{\mathbf{k}}$  to identify BCS-like versus BEC-like behavior as

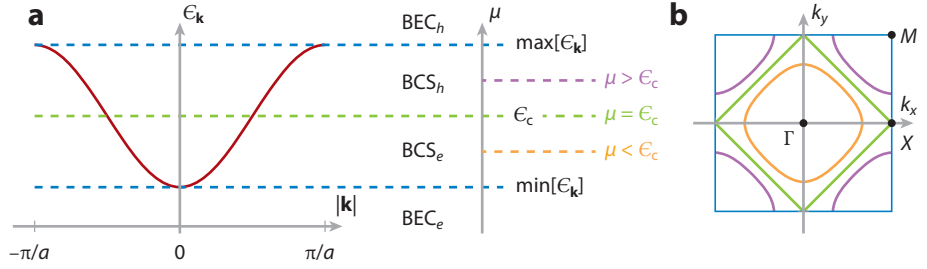


**Figure 2**

(a) Particle-like lattice dispersion  $\epsilon_{\mathbf{k}}$  and phase diagram for  $\mu$  with respect to energies  $\min[\epsilon_{\mathbf{k}}]$ ,  $\epsilon_c$ , and  $\max[\epsilon_{\mathbf{k}}]$ . Regions in the phase diagram are labeled as electron-like (particle-like) or hole-like:  $\text{BEC}_e$ ,  $\text{BCS}_e$ ,  $\text{BCS}_b$ , and  $\text{BEC}_b$ . For nodal (nodeless) order parameters, the BCS/BEC boundaries correspond to quantum phase transitions (crossovers). (b) Loci in momentum space, where  $\xi_{\mathbf{k}} = 0$ , that is,  $\epsilon_{\mathbf{k}} = \mu$ .

$\mu$  changes. As shown in **Figure 2**, four superconducting or superfluid regions, labeled as electron-like (particle-like) or hole-like, exist:  $\text{BEC}_e$ ,  $\text{BCS}_e$ ,  $\text{BCS}_b$ , and  $\text{BEC}_b$  (49). Crossovers or quantum phase transitions may occur during the evolution from the BCS to the BEC regime in 3D and 2D.

### 3. ONE-BAND BCS–BEC IN 2D: CROSSOVERS

For  $s$ -wave systems, the evolution from the BCS to the BEC regime is just a crossover (15). To establish how close the system is to the BEC regime, it is important to analyze a few properties of the system to identify where the chemical potential  $\mu$  lies. At zero temperature ( $T = 0$ ),  $\mu$  can be changed by either tuning interactions at fixed particle density  $n$  in cold-atom superfluids (10, 11, 48) or adjusting the carrier density for fixed interactions in superconductors (1–5, 7, 53).

In cold-atom experiments, it is now possible to create two-dimensional box potentials using digital micromirror devices (46), such that homogeneous two-dimensional Fermi gases can be produced (10, 11, 44), which is a major advance in getting rid of the intrinsic inhomogeneity of harmonic traps. This technical achievement allows for comparison to theoretical work that describes the crossover from BCS to BEC in 2D (32), starting from a two-dimensional continuum action,

$$S = \int_0^{\hbar/k_B T} d\tau \left[ \sum_{\mathbf{k}\sigma} \psi_{\mathbf{k}\sigma}^\dagger(\tau) (\hbar \partial_\tau + \xi_{\mathbf{k}}) \psi_{\mathbf{k}\sigma}(\tau) + \sum_{\mathbf{k}\mathbf{k}'\mathbf{q}} V_{\mathbf{k}\mathbf{k}'} b_{\mathbf{k}\mathbf{q}}^\dagger(\tau) b_{\mathbf{k}\mathbf{q}}(\tau) \right], \quad 2.$$

where  $b_{\mathbf{k}\mathbf{q}}(\tau) = \psi_{-\mathbf{k}+\frac{\mathbf{q}}{2}\downarrow}(\tau) \psi_{\mathbf{k}+\frac{\mathbf{q}}{2}\uparrow}(\tau)$  represent pairs of fermions with center of mass momentum  $\mathbf{q}$  and relative momentum  $2\mathbf{k}$ . The interaction  $V_{\mathbf{k}\mathbf{k}'}$  can be expanded in its angular momentum components (53); considering only the  $s$ -wave channel leads to the separable form  $V_{\mathbf{k}\mathbf{k}'} = \lambda \Gamma_{\mathbf{k}} \Gamma_{\mathbf{k}'}$ , with  $\Gamma_{\mathbf{k}} = (1 + |\mathbf{k}|/k_0)^{-1/2}$ . Here,  $k_0 = 2\pi/R$ , with  $R$  playing the role of the interaction range in real space. In the case of ultracold fermions, the interaction range  $R \rightarrow 0$  ( $k_0 \rightarrow \infty$ ), so it is more convenient to express the interactions in terms of the two-body bound state energy  $E_b$  as

$$\frac{1}{\lambda} = \sum_{\mathbf{k}} \frac{|\Gamma_{\mathbf{k}}|^2}{2\epsilon_{\mathbf{k}} - E_b} \quad 3.$$

or the two-dimensional scattering length  $a_{2D} = 2k_F^{-1} e^{-\gamma_E} \sqrt{2\epsilon_F/|E_b|}$ , with  $\gamma_E \approx 0.577$  being the Euler–Mascheroni constant (57). In 2D, contact  $s$ -wave interactions lead to a two-body bound state for arbitrary small  $\lambda$  (48), in contrast to 3D, where a critical value of  $\lambda$  is required to produce a two-body bound state (18, 19).

Neglecting modulus fluctuations of the order parameter, superconductivity and superfluidity emerge via the pairing field  $\Delta_r = |\Delta|e^{i\theta_r}$ , where  $r = (\mathbf{r}, \tau)$ ;  $\mathbf{r} = (x, y)$  is the real space position and  $\tau$  is the imaginary time. The modulus of the order parameter is  $|\Delta|$  and  $\theta_r$  represents phase fluctuations. In momentum space, the order parameter is  $\Delta_{\mathbf{k}} = |\Delta|\Gamma_{\mathbf{k}}$  and the phase-only effective action is

$$S_{\text{fl}} = \frac{1}{2} \int d^3r \{ \rho_{ij} \partial_i \theta_r \partial_j \theta_r + A [\hbar \partial_\tau \theta_r]^2 \}, \quad 4.$$

where the indices  $i$  and  $j$  cover the set  $\{x, y\}$ . The superfluid stiffness tensor  $\rho_{ij}$ , with dimensions of energy, and  $A$ , related to the isothermal compressibility, are functions of temperature  $T$ , order parameter modulus  $|\Delta|$ , and chemical potential  $\mu$ . For isotropic systems,  $\rho_{ij} = \rho \delta_{ij}$ , the Berezinskii–Kosterlitz–Thouless (BKT) temperature (58, 59) is given by the Nelson–Kosterlitz (59, 60) relation  $k_B T_{\text{BKT}} = \pi \rho / 2$ , whereas for anisotropic systems, with  $\rho_{ij} = \rho_{ii} \delta_{ij}$ ,  $k_B T_{\text{BKT}} = \pi \sqrt{\rho_{xx} \rho_{yy}} / 2$  (61, 62). It should be emphasized that  $T_{\text{BKT}}$  is a function of  $\mu$ ,  $|\Delta|$ , and  $E_b$  (32) and of the source of the anisotropy in  $\rho_{ij}$ , like spin–orbit coupling (61, 62). For a Galilean invariant system, with  $\epsilon_{\mathbf{k}} = \hbar^2 \mathbf{k}^2 / 2m$ , the superfluid stiffness  $\rho$  is always bounded by  $\hbar^2 n / 4m$ . Using  $n = k_F^2 / 2\pi$  leads to an upper bound on the BKT temperature  $T_{\text{BKT}} \leq T_F / 8 = 0.125 T_F$  (48), where  $T_F = E_F / k_B$  and  $E_F = \hbar^2 k_F^2 / 2m$  are the Fermi temperature and energy, respectively. The same bound also applies to anisotropic  $\rho_{ij}$ , caused, for example, by spin–orbit coupling, because the action  $S_{\text{fl}}$  is conformally invariant. So, Equation 4 can be brought into its diagonal scalar form by conformal transformations, rotation, and scaling of coordinates, producing the same bound (61, 62). An example of the BKT temperature for zero-ranged (contact) interactions is shown in **Figure 3**, together with the mean-field temperature, where  $|\Delta| = 0$ .

Theories that invoke phase fluctuations only cannot describe the deeply bound regime where  $|E_b|/E_F \gg 1$  because they neglect modulus fluctuations of the order parameter. The inclusion of Gaussian corrections from the modulus fluctuations are still not sufficient, because they just renormalize the compressibility and leave the superfluid stiffness unchanged. It is still an open question how to construct a microscopic theory that recovers the Fisher–Hohenberg logarithmic corrections to the critical temperature  $T_c$ , coming from interactions between the bosonic degrees of freedom (63) linked to deeply bound states. One can add phenomenologically or ad hoc the contributions that produce the Fisher–Hohenberg logarithmic corrections, but that does not provide a microscopic theory.

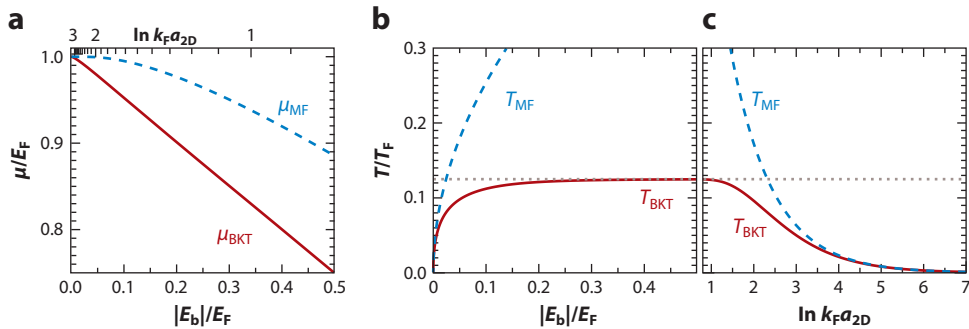


**Figure 3**

(a) Chemical potential  $\mu/E_F$  versus binding energy  $|E_b|/E_F$  and two-dimensional scattering length  $\ln k_F a_{2D}$  at the mean-field (MF) and BKT temperatures. (b) Mean-field ( $T_{\text{MF}}$ ) and BKT ( $T_{\text{BKT}}$ ) temperatures versus  $|E_b|/E_F$ . (c)  $T_{\text{MF}}$  and  $T_{\text{BKT}}$  versus  $\ln k_F a_{2D}$ . The theoretical upper bound  $T_F/8$  is shown as a dotted gray line. Figure adapted from Reference 32. Abbreviation: BKT, Berezinskii–Kosterlitz–Thouless.

### 3.1. Superfluids in 2D: Ultracold Fermi Atoms in Box Potentials

In ultracold Fermi superfluids, there are several ways to probe the consequences of a BCS–BEC crossover in 3D and 2D. In the past, quantitative comparisons between theory and experiment were difficult, because most theoretical work was done in continuum homogeneous systems, whereas experiments always had some degree of harmonic confinement, making the Fermi superfluids inhomogeneous. Theories that include the effects of harmonic confinement (64, 65) rely mostly on the local density approximation, leading to mixed results (41, 42), so making contact with experiments using harmonic traps (39, 40) may be unreliable. With the advent of two-dimensional box potentials, it has become easier to compare experimental results with theoretical predictions. For instance, an experiment with inhomogeneous two-dimensional systems has reported a critical temperature  $T_c$  (39) that seems to exceed the known theoretical upper bound  $T_c = T_F/8$ , based on the BKT mechanism. If the measurement of  $T_c$  is correct, this would suggest that inhomogeneous systems can have higher  $T_c$  than the upper bound for homogeneous systems. Conversely, this also raises questions about having accurate thermometry, which has been an issue for cold-atom systems for a long time (66, 67). Box potentials in 2D (44, 46) and improved thermometry using machine learning (68) may lead to an accurate determination of  $T_c$  as a function of the binding energy  $E_b$  or scattering length  $a_{2D}$  while providing a test bed for the applicability of the BKT mechanism to two-dimensional Fermi superfluids.

In cold-atom systems, it is possible to directly probe the energy spectrum using two-photon Bragg spectroscopy (11). This technique uses two laser pulses to excite the atoms through absorption and stimulated emission of two photons. The energy and momentum that is transferred to the gas can be chosen by selecting the specific frequency and relative position of the two lasers; by measuring the response of the system, the dynamical structure factor can be inferred (11). The dynamical structure factor is a measure of the density–density response of the superfluid, which provides information about the many-particle energy spectrum. Specifically, it can probe the low-energy collective modes that arise from the spontaneously broken U(1) symmetry. At energies larger than twice the gap of the quasiparticles, it is energetically favorable to break pairs, such that the dynamical structure factor explores the two-particle continuum. Interestingly, in 2D, the collective modes exist for all wave numbers, in contrast to 3D, where higher-momentum modes can get damped by breaking up in the two-particle continuum below a certain interaction strength (69, 70). This is a result of the presence of two-body bound states for all  $s$ -wave contact interactions in 2D (71). As more experiments are being done in homogeneous potentials (11, 51), the agreement with the continuum theory is very good, improving our understanding of two-dimensional superfluids as they evolve from the BCS to BEC regime. In **Figure 4**, the low-energy collective modes are shown for different values of  $\mu$  (71). In the BCS regime, the dispersion is pushed down by the two-particle continuum but never reaches it in 2D.

### 3.2. Superconductors in 2D: Lack of One-Band BCS–BEC Crossover Experiments

Whereas ultracold atoms have provided clean experimental examples of the crossover from the BCS to BEC regimes in 3D and 2D, such manifestations are still lacking for one-band superconductors due to technical difficulties. In ultracold atoms, such as  ${}^6\text{Li}$  and  ${}^{40}\text{K}$ , the densities can be quite low, but the interactions can be changed with the help of Feshbach–Fano (28, 29) resonances. The tuning of attractive interactions between Fermi atoms from weak to strong may force the chemical potential to change from  $\mu > 0$  to  $\mu < 0$  and may induce a BCS–BEC crossover in Fermi superfluids with  $\epsilon_{\mathbf{k}} = \hbar^2 \mathbf{k}^2 / 2m$ . This wide-range tuning of interactions is not currently possible in superconductors, where often the type, strength, or range of the interactions that lead

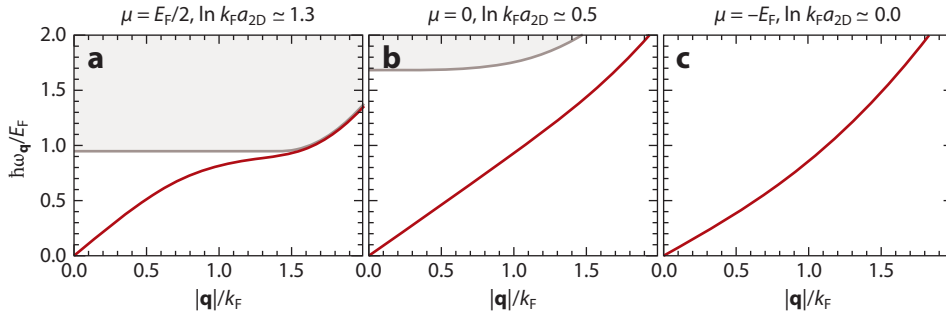


**Figure 4**

Collective mode dispersion  $\hbar\omega_{\mathbf{q}}/E_F$  versus  $|\mathbf{q}|/k_F$  for different values of  $\mu/E_F$ . In the BCS limit, when  $\mu/E_F \approx 1$ , the sound velocity is  $c \approx v_F/\sqrt{2}$ . In the BEC limit, where  $\mu/E_F \approx -|E_b|/2E_F$ , the sound velocity is  $c \approx v_F/\sqrt{8|\ln k_F a_{2D}|}$ . A comparison between theory (71) and experiments in  ${}^6\text{Li}$  (11) shows excellent agreement. The binding energy and sound velocity in the different panels are: (a)  $E_b \simeq 0.2E_F$ ,  $c \simeq 0.55v_F$ ; (b)  $E_b \simeq 0.8E_F$ ,  $c \simeq 0.46v_F$ ; (c)  $E_b \simeq 2.5E_F$ ,  $c \simeq 0.37v_F$ .

to superconductivity are not known. So, the tuning of  $\mu$  for one-band superconductors can only be achieved by changing the carrier density, via either chemical doping or electrostatically with gating techniques. Thus far, there are no clear experimental examples in which the crossover from BCS to BEC occurs in one-band two-dimensional superconductors, in either the continuum or the lattice. For instance, even the switch from BCS<sub>e</sub> to BCS<sub>b</sub> at half-filling shown in **Figure 2a** may be absent because of competing phases, such as the antiferromagnetic insulator. The evolution from BCS<sub>e</sub> to BEC<sub>e</sub> or BCS<sub>b</sub> to BEC<sub>b</sub> may not occur because carrier densities are not sufficiently low or high and interactions may not be sufficiently strong to push  $\mu$  below  $\min[\epsilon_{\mathbf{k}}]$  or above  $\max[\epsilon_{\mathbf{k}}]$ . However, as we discuss in Sections 6 and 7, there are some promising two-band and multiband materials for which experimental work suggests that the BCS–BEC evolution may be within reach.

#### 4. ONE-BAND BCS–BEC IN 2D: QUANTUM PHASE TRANSITIONS

Although crossovers are interesting, they are not as striking as quantum phase transitions, in which dramatic physical signatures arise close to the transition point, line, or surface. For higher angular momentum  $\ell$ , the formal expressions for the action  $S$ , two-body bound state energy  $E_b$ , and phase-only effective action  $S_{\text{fl}}$  are exactly the same as those in Equations 2–4, with the simple change  $\Gamma_{\mathbf{k}} = \gamma_{|\mathbf{k}|}^{2D} \cos \ell\phi$ , where  $\gamma_{|\mathbf{k}|}^{2D} = (|\mathbf{k}|/k_1)^\ell / (1 + |\mathbf{k}|/k_0)^{\ell+1/2}$ . The low-momentum scale is set by  $k_1$ , whereas the momentum range is set by  $k_0 = 2\pi/R$ , leading to low and high momentum behavior of  $V_{\mathbf{k}\mathbf{k}'}$  compatible with a physically acceptable real space interaction (53). The momentum scale  $k_1$  can always be absorbed into the strength  $\lambda$  of the interactions and into the modulus  $|\Delta|$  of the order parameter, so the choice  $k_1 = k_0$  can be made without loss of generality.

As discussed in Section 2, interactions beyond  $s$ -wave ( $\ell = 0$ ) may lead to quantum phase transitions in superconductors and superfluids in which  $E_{\mathbf{k}}$  is gapless in the BCS and gapped in the BEC regimes. In **Figure 5a**,  $\min[E_{\mathbf{k}}]$  versus  $\mu$  is shown for  $\ell = 2$  ( $d$ -wave), where  $\min[E_{\mathbf{k}}] = |\mu|$  for  $\mu < 0$  and  $\min[E_{\mathbf{k}}] = 0$  for  $\mu > 0$ . In **Figure 5b**, the nodal structure of the order parameter  $\Delta_{\mathbf{k}} = |\Delta|\gamma_{|\mathbf{k}|}^{2D} \cos 2\phi$  with  $d_{x^2-y^2}$  symmetry is displayed for  $\mu > 0$ , revealing the Dirac points at  $\phi = \pi/4 + n\pi/2$  for  $n \in \{0, 1, 2, 3\}$ . For  $\ell = 2$ , the function  $\gamma_{|\mathbf{k}|}^{2D} = (|\mathbf{k}|/k_1)^2 / (1 + |\mathbf{k}|/k_0)^{5/2}$  defines the low and high momentum behavior and  $\cos 2\phi$  defines the nodal structure of the order parameter. Even though time-reversal symmetry is not broken, the emerging Dirac fermions for

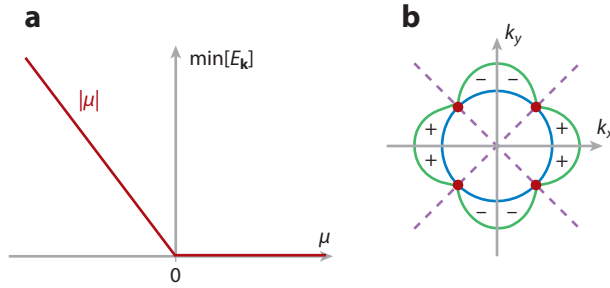


**Figure 5**

(a) Sketch of  $\min[E_{\mathbf{k}}]$  versus  $\mu$  for  $\ell = 2$  ( $d$ -wave): for  $\mu > 0$ ,  $E_{\mathbf{k}}$  is gapless with  $\min[E_{\mathbf{k}}] = 0$ ; for  $\mu < 0$ ,  $E_{\mathbf{k}}$  is gapped with  $\min[E_{\mathbf{k}}] = |\mu|$ . (b) The nodal structure of  $\Delta_{\mathbf{k}} = \Delta\gamma_{|\mathbf{k}|}^{2D} \cos 2\phi$  at  $\mathbf{k}_{\mu}$  for  $\mu > 0$ , showing the four Dirac points at  $\phi = \pi/4 + n\pi/2$  with  $n \in \{0, 1, 2, 3\}$ .

$\mu > 0$  are chiral and have winding numbers

$$N_w = \frac{1}{2\pi} \oint_C d\ell \hat{\mathbf{z}} \cdot \mathbf{m} \times \frac{d\mathbf{m}}{d\ell}, \quad 5.$$

where  $\mathbf{m} = (\xi_{\mathbf{k}}, \Delta_{\mathbf{k}})/E_{\mathbf{k}}$ , and  $C$  is a counterclockwise path that encircles each individual Dirac point. The winding number  $N_w$  alternates between  $-1$  ( $\phi = \pi/4, 5\pi/4$ ) and  $+1$  ( $\phi = 3\pi/4, 7\pi/4$ ). Because there is no global chiral symmetry breaking, the net chirality of the system is always zero. Nevertheless, the tuning of  $\mu \rightarrow 0$  forces the annihilation of these chiral Dirac fermions, producing a topological quantum phase transition in momentum space exactly at  $\mu = 0$ . For  $\mu < 0$ ,  $E_{\mathbf{k}}$  is gapped, with  $\min[E_{\mathbf{k}}] = |\mu|$  at  $|\mathbf{k}| = 0$ , and  $N_w$  is always zero, because chiral Dirac fermions no longer exist.

The topological quantum phase transition caused by the annihilation of Dirac quasiparticles is analogous to the Lifshitz transition in ordinary metals (72), as seen in **Figure 6**, where plots of the quasiparticle/quasihole energies  $\pm E_{\mathbf{k}}$  are shown for three values of  $\mu$ . The qualitative differences in the excitation spectrum  $E_{\mathbf{k}}$  have dramatic effects in the momentum distributions and density of states (53, 55). Such changes in  $E_{\mathbf{k}}$  produce a similar but stronger effect when compared to the standard Lifshitz transition, where the Fermi surface of metals may change as a function of pressure, with the breaking of a neck in the Fermi surface at a critical pressure. For instance, the isothermal compressibility  $n^2 \kappa_T = dn/d\mu|_T$  of a  $d$ -wave superconductor or superfluid exhibits a

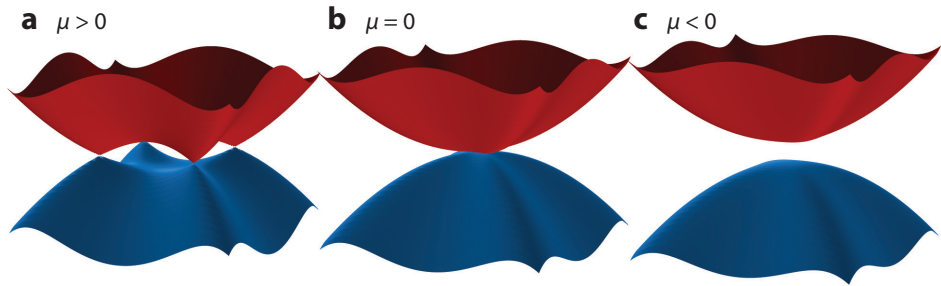


**Figure 6**

Quasiparticle (red) and quasihole (blue) energies  $\pm E_{\mathbf{k}}$  showing the annihilation of the Dirac points as  $\mu$  evolves from positive to negative. At  $\mu = 0$ , the chiral Dirac fermions annihilate, and a topological quantum phase transition occurs. Figure adapted from Reference 48.

logarithmic singularity as  $\mu \rightarrow 0$  (48, 53). This is in sharp contrast to the conventional Lifshitz transition, where  $\kappa_T$  is continuous, but its derivative with respect to pressure has a square-root divergence as the critical pressure is approached (53, 72).

For a lattice with particle-like dispersion  $\epsilon_{\mathbf{k}} = -2t(\cos k_x a + \cos k_y a)$  and an order parameter with  $d$ -wave symmetry  $\Delta_{\mathbf{k}} = |\Delta|(\cos k_x a - \cos k_y a)$ , two topological quantum phase transitions occur: one from  $\text{BCS}_e$  to  $\text{BEC}_e$  when  $\mu = \min[\epsilon_{\mathbf{k}}]$  and the other from  $\text{BCS}_b$  to  $\text{BEC}_b$  when  $\mu = \max[\epsilon_{\mathbf{k}}]$ . In both cases, chiral Dirac fermions annihilate at the critical values of  $\mu$  and are responsible for the topological quantum phase transitions. Due to the  $d$ -wave ( $d_{x^2-y^2}$ ) nature of the order parameter, when the BCS–BEC evolution occurs in these systems, it is inevitable that it must encounter a topological quantum critical point at  $T = 0$  and that it must sense the existence of this topological quantum critical point at finite temperatures (48, 53). An important thermodynamic signature of this topological quantum critical point is the logarithmic singularity of the isothermal compressibility  $n^2 \kappa_T$  at the critical chemical potential  $\mu_c$ , where the chiral Dirac quasiparticles annihilate; that is,  $\mu_c = \min[\epsilon_{\mathbf{k}}]$  or  $\mu_c = \max[\epsilon_{\mathbf{k}}]$ . At  $T = 0$ ,  $n^2 \kappa_T \approx -\alpha \ln [|\mu - \mu_c|/E_0] + \beta$ , where  $E_0 = \hbar^2 k_0^2/2m$  is the energy unit and  $\alpha$  ( $\beta$ ) is independent of (dependent on) the sign of  $\mu - \mu_c$  (53). At nonzero  $T$ , the proximity to this topological quantum critical point manifests itself as a maximum in  $n^2 \kappa_T$  at the corresponding values of  $\mu(T) = \min[\epsilon_{\mathbf{k}}]$  or  $\mu(T) = \max[\epsilon_{\mathbf{k}}]$ . Such a topological quantum critical point was entirely missed in early work on the BCS–BEC evolution in 2D (73), but it was identified accurately in later work (53–55, 74).

For the BCS–BEC evolution, the critical BKT temperatures have been calculated for nodal order parameters (e.g.,  $p$ - and  $d$ -wave) (56). Within a phase-only fluctuation theory,  $T_{\text{BKT}}$  were shown to increase as functions of interaction strength or particle density and to have the same bound  $T_{\text{BKT}} \leq T_{\text{F}}/8$  as the  $s$ -wave case (48). More recently, these results were rediscovered and extended (75), but they are all based on phase-only actions, which cannot recover the Fisher–Hohenberg logarithmic corrections in  $T_c$  when the Bose regime is reached.

Although there are candidates for topological quantum phase transitions in one-band two-dimensional superconductors and superfluids, its unquestionable experimental observation remains elusive. In the context of superconductors, the high-critical-temperature cuprates are natural systems to explore, because they are essentially two-dimensional, are known to have  $d$ -wave ( $d_{x^2-y^2}$ ) symmetry, and thus satisfy the higher angular momentum pairing requirement. They also have preformed pairs at low doping, suggesting that the interaction strength could be sufficiently strong to allow for the chemical potential to cross its critical value where the gapless  $d$ -wave excitations become fully gapped. Even though it was recently suggested that there is a BCS–BEC evolution in the cuprates (76), based on specific heat measurements near the critical temperature, this argument has been countered (77) by the fact that similar experiments do not show signatures of a quantum phase transition at low temperatures, like the logarithmic singularity in the compressibility or the collapse of Dirac fermions in the momentum distribution (48, 53). There are also possible topological quantum phase transitions in systems with higher angular momentum pairing that break time-reversal symmetry, such as  $p$ -wave ( $p_x + ip_y$ ), when the chemical potential falls below the bottom or rises above the top of the band in a lattice or falls below the bottom of the band in the continuum (74). These systems are not gapless with chiral Dirac fermions in the bulk; rather they are fully gapped with Majorana fermions at the sample boundaries in the BCS regime, and their BEC phase is also gapped. These Majorana edge modes are the hallmark of gapped topological superconductors. However, current experimental candidates in 2D, such as interfaces between quantum Hall insulators and niobium, do not yet present undisputed evidence of Majorana modes (78) or of the sought-after topological quantum phase transition.

For ultracold atoms, BCS–BEC topological quantum phase transitions have been theoretically suggested for two-dimensional  $p$ -wave systems with ( $p_x$  or  $p_y$ ) or without nodes ( $p_x + ip_y$ ), where time-reversal symmetry is preserved or broken (48, 79). However, the lifetimes of atom pairs are experimentally too short, due to collisional losses and dissociation through the centrifugal barrier (30), and superfluidity has never been observed in  $p$ -wave Fermi gases, such as  ${}^6\text{Li}$  or  ${}^{40}\text{K}$ , in either 3D or 2D. However, there is hope that the lifetimes of these pairs can be substantially increased by trapping  $p$ -wave fermions in either a box potential (46) or a lattice (80), where collisional losses can be substantially reduced.

## 5. ROLE OF CHEMICAL POTENTIALS IN TWO-BAND SYSTEMS

In two-band systems, the chemical potential also plays a very important role in the evolution from BCS to BEC superconductivity or superfluidity. Considering two particle-like bands  $\epsilon_{1\mathbf{k}} = \epsilon_{10} + \hbar^2\mathbf{k}^2/2m_1$  and  $\epsilon_{2\mathbf{k}} = \epsilon_{20} + \hbar^2\mathbf{k}^2/2m_2$ , attractive intraband interactions  $\lambda_{11}$  and  $\lambda_{22}$ , and interband interactions  $\lambda_{12}$  of the Josephson type leads to quasiparticle energy dispersions

$$E_{1\mathbf{k}} = \sqrt{\xi_{1\mathbf{k}}^2 + |\Delta_{1\mathbf{k}}|^2} \quad \text{and} \quad E_{2\mathbf{k}} = \sqrt{\xi_{2\mathbf{k}}^2 + |\Delta_{2\mathbf{k}}|^2}. \quad 6.$$

Here,  $\xi_{j\mathbf{k}} = \epsilon_{j\mathbf{k}} - \mu_j$  are the independent particle energies  $\epsilon_{j\mathbf{k}}$  with respect to chemical potentials  $\mu_j$ , and  $\Delta_{j\mathbf{k}} = |\Delta_j|\Gamma_{j\mathbf{k}}$  are order parameters in band  $j$ , where  $\Gamma_{j\mathbf{k}}$  contains the angular momentum symmetry factor. Within pairing theories, the discussion below is general, provided that  $|\Delta_j| \neq 0$  and that no competing phases have lower free energy than the superfluid or superconducting state. For conductors in standard condensed matter systems, only the total number of particles can be fixed, thus  $\mu_1 = \mu_2 = \mu$ . However, for cold atoms, the chemical potentials  $\mu_1$  and  $\mu_2$  can be different, because the number of particles in each band may be fixed independently (81, 82).

In close analogy to the one-band case, we can immediately infer the BCS and BEC regions by analyzing the chemical potentials  $\mu_j$  with respect to the minima of  $\epsilon_{j\mathbf{k}}$  as seen in **Figure 7**. For particle-like parabolic bands  $\epsilon_{1\mathbf{k}} = \epsilon_{10} + \hbar^2\mathbf{k}^2/2m_1$  and  $\epsilon_{2\mathbf{k}} = \epsilon_{20} + \hbar^2\mathbf{k}^2/2m_2$ , with  $\epsilon_{10} \geq \epsilon_{20}$ , the energies  $\xi_{1\mathbf{k}} = \epsilon_{1\mathbf{k}} - \mu_1$  and  $\xi_{2\mathbf{k}} = \epsilon_{2\mathbf{k}} - \mu_2$  can be simply rewritten as  $\xi_{j\mathbf{k}} = \hbar^2\mathbf{k}^2/2m_j - \tilde{\mu}_j$ , where  $\tilde{\mu}_j = \mu_j - \min[\epsilon_{j\mathbf{k}}] = \mu_j - \epsilon_{j0}$ . For band  $j$ , the regimes are BCS $_j$  for  $\tilde{\mu}_j > 0$  and BEC $_j$  for  $\tilde{\mu}_j < 0$ , with crossovers from BCS $_j$  to BEC $_j$  occurring around  $\tilde{\mu}_j = 0$  in the  $s$ -wave channel, and topological quantum phase transitions occurring at  $\tilde{\mu}_j = 0$  in higher angular momentum channels (e.g.,  $p$ -wave or  $d$ -wave). If  $\tilde{\mu}_1$  and  $\tilde{\mu}_2$  can be tuned independently, then there are four possible cases: (a) BCS $_1$ -BCS $_2$  for  $\tilde{\mu}_1 > 0$  and  $\tilde{\mu}_2 > 0$ ; (b) BEC $_1$ -BCS $_2$  for  $\tilde{\mu}_1 < 0$  and  $\tilde{\mu}_2 > 0$ ; (c) BCS $_1$ -BEC $_2$  for  $\tilde{\mu}_1 > 0$  and  $\tilde{\mu}_2 < 0$ ; and (d) BEC $_1$ -BEC $_2$  for  $\tilde{\mu}_1 < 0$  and  $\tilde{\mu}_2 < 0$ , as seen in **Figure 7a**. Analogously, for a two-band system with one electron-like (particle-like) band  $\epsilon_{e\mathbf{k}} = \epsilon_{e0} + \hbar^2\mathbf{k}^2/2m_e$

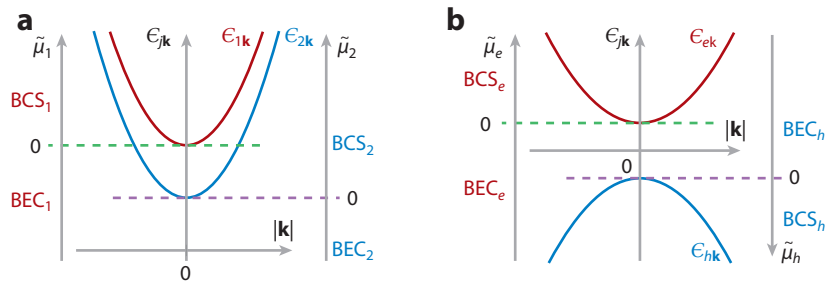


**Figure 7**

(a) Parabolic particle-like bands  $\epsilon_{1\mathbf{k}}$  and  $\epsilon_{2\mathbf{k}}$  and phase diagram for  $\tilde{\mu}_1$  and  $\tilde{\mu}_2$ . (b) Parabolic electron and hole bands  $\epsilon_{e\mathbf{k}}$  and  $\epsilon_{h\mathbf{k}}$  and phase diagram for  $\tilde{\mu}_e$  and  $\tilde{\mu}_h$ .

and one hole-like band  $\epsilon_{bk} = -\epsilon_{bg}/2 - \hbar^2 \mathbf{k}^2/2m_b$ , the energies  $\xi_{ek} = \epsilon_{ek} - \mu_e$  and  $\xi_{bk} = \epsilon_{bk} + \mu_b$  become  $\xi_{ek} = \hbar^2 \mathbf{k}^2/2m_e - \tilde{\mu}_e$  and  $\xi_{bk} = -\hbar^2 \mathbf{k}^2/2m_b + \tilde{\mu}_b$ , where the shifted chemical potentials are  $\tilde{\mu}_e = \mu_e - \epsilon_{bg}/2$  and  $\tilde{\mu}_b = \mu_b - \epsilon_{bg}/2$ . If  $\tilde{\mu}_e$  and  $\tilde{\mu}_b$  can be tuned independently, then there are again four possible cases: (a) BCS<sub>e</sub>-BCS<sub>b</sub> for  $\tilde{\mu}_e > 0$  and  $\tilde{\mu}_b > 0$ ; (b) BEC<sub>e</sub>-BCS<sub>b</sub> for  $\tilde{\mu}_e < 0$  and  $\tilde{\mu}_b > 0$ ; (c) BCS<sub>e</sub>-BEC<sub>b</sub> for  $\tilde{\mu}_e > 0$  and  $\tilde{\mu}_b < 0$ ; and (d) BEC<sub>e</sub>-BEC<sub>b</sub> for  $\tilde{\mu}_e < 0$  and  $\tilde{\mu}_b < 0$ , as illustrated in **Figure 7b**. For order parameters that do not break time-reversal symmetry, crossovers occur among these four different regions for nonnodal order parameters (e.g., *s*-wave), whereas topological quantum phase transitions arise for nodal order parameters (e.g., *d*-wave). For lattice energies  $\epsilon_{jk}$ , including two particle-like or one particle-like and one hole-like dispersions, the situation is similar to the one-band case shown in **Figure 2**. See also Section 9, where an outlook is discussed for two bands in lattices.

## 6. TWO-BAND BCS–BEC IN 2D: CROSSOVERS

A few experimental two-band or multiband systems in 2D are candidates for the BCS–BEC crossover in the condensed matter setting. One example is multiband layered superconductors such as FeSe (6, 7) and FeSe<sub>1-x</sub>S<sub>x</sub> (8, 9), where spectroscopic evidence exists from photoemission experiments that one of the quasihole bands in the superconducting state changes from gapped at nonzero momentum to gapped at zero momentum as a function of doping *x* (8), a hallmark of the crossover from BCS to BEC. In addition to changing carrier concentration, chemical doping can introduce other effects, such as disorder or structural phase transitions, which may mask the evolution from BCS to BEC. Recently, however, it has been possible to use gating to change the carrier density *n* in layered nitrides (1, 2), where disorder or structural phase transitions do not seem to be important. Because *n* can vary from low to high values, it is crucial to consider the effects of the interaction range *R*, as it can become comparable to or larger than typical interparticle spacings. Furthermore, it is necessary to verify that the carrier densities achieved by gating are sufficiently low to force the chemical potential below the minimum of particle-like bands or above the maximum of hole-like bands, otherwise BCS–BEC crossovers do not happen.

Starting from a two-dimensional continuum action with two bands

$$S_{2B} = \int_0^{\hbar/k_B T} d\tau \left[ \sum_{j\mathbf{k}\mathbf{s}} \psi_{j\mathbf{k}\mathbf{s}}^\dagger(\tau) (\hbar\partial_\tau + \xi_{j\mathbf{k}}) \psi_{j\mathbf{k}\mathbf{s}}(\tau) + \sum_{ij\mathbf{k}\mathbf{k}'\mathbf{q}} V_{\mathbf{k}\mathbf{k}'}^{ij} b_{i\mathbf{k}\mathbf{q}}^\dagger(\tau) b_{j\mathbf{k}\mathbf{q}}(\tau) \right], \quad 7.$$

where  $\xi_{j\mathbf{k}} = \epsilon_{j\mathbf{k}} - \mu_j$  is the kinetic energy  $\epsilon_{j\mathbf{k}}$  with respect to  $\mu_j$ ,  $b_{j\mathbf{k}\mathbf{q}}(\tau) = \psi_{j-\mathbf{k}+\frac{\mathbf{q}}{2}\downarrow}(\tau) \psi_{j\mathbf{k}+\frac{\mathbf{q}}{2}\uparrow}(\tau)$  represent pairs of fermions at band *j* with center of mass momentum  $\mathbf{q}$  and relative momentum  $2\mathbf{k}$ , and the interaction  $V_{\mathbf{k}\mathbf{k}'}^{ij}$  can be expanded in its angular momentum components (53). Considering a single angular momentum channel leads to the separable form  $V_{\mathbf{k}\mathbf{k}'}^{ij} = \lambda_{ij} \Gamma_{i\mathbf{k}} \Gamma_{j\mathbf{k}'}$ . For *s*-wave pairing,  $\Gamma_{j\mathbf{k}} = (1 + |\mathbf{k}|/k_0)^{-1/2}$ , where  $k_0 = 2\pi/R$ , such that *R* plays the role of the interaction range in real space. For any interaction range *R*, it is convenient to express the interactions in terms of the two-body bound state energies  $E_{j\mathbf{b}}$  as

$$\frac{1}{\lambda_{jj}} = \sum_{\mathbf{k}} \frac{|\Gamma_{j\mathbf{k}}|^2}{2\epsilon_{j\mathbf{k}} - E_{j\mathbf{b}}}. \quad 8.$$

In 2D, *s*-wave interactions lead to a two-body bound state for arbitrarily small  $\lambda_{jj}$  (32), but a critical value of  $\lambda_{jj}$  is required in the *d*-wave channel (53).

Considering the interband interaction  $\lambda_{12}$  to be Josephson-like, the phase-only fluctuation action is

$$S_{\Pi} = \sum_{j=1}^2 \frac{1}{2} \int d^3 r \left[ \rho_{jj} (\nabla\theta_{jr})^2 + A_j (\hbar\partial_\tau \theta_{jr})^2 \right] + 2g_{12} \int \frac{d^3 r}{L^2} |\Delta_1| |\Delta_2| \cos(\theta_{1r} - \theta_{2r}), \quad 9.$$

where the bare superfluid stiffness tensor  $\rho_{ij} = \rho_{jj}\delta_{ij}$ , which has dimensions of energy, is labeled by the band indices  $\{i, j\}$ ;  $A_j$  is related to the isothermal compressibility in band  $j$ ; and  $g_{12}$  represents the Josephson coupling between the order parameters  $\Delta_{1r} = |\Delta_1|e^{i\theta_{1r}}$  and  $\Delta_{2r} = |\Delta_2|e^{i\theta_{2r}}$ . For the two-band case, there are at least two critical BKT temperatures:  $k_B T_{1\text{BKT}} = \rho_{11}\pi/2$  for vortex–antivortex binding in  $\theta_{1r}$  only, and  $k_B T_{2\text{BKT}} = \rho_{22}\pi/2$  for vortex–antivortex binding in  $\theta_{2r}$  only. More generally, the critical temperature is (83)

$$k_B T_{\text{BKT}}(n_1, n_2) = [\rho_{11}n_1^2 + \rho_{22}n_2^2 + 2\rho_{12}n_1n_2] \frac{\pi}{2}, \quad 10.$$

where  $n_j \in \{0, \pm 1\}$  represents the vortex or antivortex topological charge associated with  $\theta_{jr}$ . For instance,  $k_B T_{\text{BKT}}(\pm 1, 0) = k_B T_{1\text{BKT}} = \rho_{11}\pi/2$ , while  $k_B T_{\text{BKT}}(0, \pm 1) = k_B T_{2\text{BKT}} = \rho_{22}\pi/2$ . Yet, there are additional possibilities, with simultaneous vortex–antivortex binding in  $\theta_{1r}$  and  $\theta_{2r}$ , depending on the sign of  $\rho_{12}$ , which originates from the Josephson coupling between the two bands. In this case,  $k_B T_{\text{BKT}}(\pm 1, \pm 1) = k_B T_{1\text{BKT}} + k_B T_{2\text{BKT}} + \rho_{12}\pi$  and  $k_B T_{\text{BKT}}(\pm 1, \mp 1) = k_B T_{1\text{BKT}} + k_B T_{2\text{BKT}} - \rho_{12}\pi$  must both be lower than  $\min[T_{1\text{BKT}}, T_{2\text{BKT}}]$ , due to the additional vortex–antivortex binding stabilized by  $\rho_{12}$  (83). If the latter condition is not satisfied, then the additional phases do not exist. When the two bands have equivalent dispersions ( $\epsilon_{1\mathbf{k}} = \epsilon_{2\mathbf{k}}$ ) and the intraband interactions are the same ( $\lambda_{11} = \lambda_{22}$ ), then the conditions  $\rho_{11} = \rho_{22} = \rho$  and  $|\rho_{12}| \ll \rho$  lead to only one critical temperature:  $T_{1\text{BKT}} = T_{2\text{BKT}} = T_{\text{BKT}}$ .

### 6.1. Two-Band Superconductors in 2D: The Case of $\text{Li}_x\text{ZrNCl}$

The Li-doped nitride  $\text{Li}_x\text{ZrNCl}$  has a two-dimensional hexagonal Brillouin zone with two identical parabolic bands centered at points  $K$  and  $K'$ . The Li-doping concentration  $x$  can be tuned through gate voltages. The effective mass of the carriers in each band is  $m$ , and the carrier density per band is  $n = x/A_{\text{cell}}$ , where  $A_{\text{cell}} = a^2 \sin \pi/3$  is the area of the unit cell of  $\text{Li}_x\text{ZrNCl}$ . The Li concentration  $x$  is connected to the Fermi energy  $E_F = \hbar^2 k_F^2/2m$  via the relation  $x = k_F^2 A_{\text{cell}}/2\pi = 2mE_F A_{\text{cell}}/2\pi \hbar^2$ . For high experimental values of  $x$ , the Li ions go deeper into the sample, and the system becomes three-dimensional. In  $\text{Li}_x\text{ZrNCl}$  there is only one critical temperature measured (1, 2), and because the two-bands are degenerate, this signals that additional phases due to interband vortex–antivortex binding are absent. For different values of  $x$ , data of the tunneling conductance  $dI/dV$  suggest that the moduli of the order parameters are identical ( $|\Delta_1| = |\Delta_2| = |\Delta|$ ) in the two degenerate bands, because only two peaks are observed. Furthermore, the experimental data also imply that the order parameters are nodeless ( $s$ -wave), because the  $dI/dV$  characteristics have typical U shapes with well-defined gaps for all values of  $x$  (1).

A comparison to experimental results in the two-dimensional regime can be made using the two-band theoretical framework reviewed above with  $\Delta_{1\mathbf{k}} = \Delta_{2\mathbf{k}} = |\Delta|\Gamma_{\mathbf{k}}$ , where  $\Gamma_{\mathbf{k}} = (1 + |\mathbf{k}|/k_0)^{-1/2}$ , and  $g_{12} = 0$ . In **Figure 8**, the experimental data, the standard  $T_c$  upper bound ( $T_F/8$ ), and the  $T_c$  obtained for zero-ranged interactions are shown, as are curves for the best fit to the data in the two-dimensional regime. The shaded regions show the values of  $x$  for which Li ions go deeper into the sample, thus making the superconductor reach a three-dimensional regime. The interaction range is  $k_0 = 0.4339/a$  ( $R = 2.305a$ ), where  $a$  is the lattice parameter, and the interaction strength is  $\lambda = 0.7090\mathcal{D}_{2D}$ , where  $\mathcal{D}_{2D} = mL^2/\pi \hbar^2$  is the constant density of states per band in 2D. This value of  $\lambda$  produces a binding energy of  $E_b/E_0 = -0.008499$ , where  $E_0 = \hbar^2 k_0^2/2m$  is the energy and  $T_0 = E_0/k_B = 1,105$  K is the temperature scale.

A measure of the crossover region around  $\mu = 0$  can be identified via the dimensionless pair size  $k_F \xi_{\text{pair}}$ . The crossover region from BCS to BEC pairing can be identified with the range  $0.5 < k_F \xi_{\text{pair}} < 5.0$  (19), corresponding to either  $-0.7898 < \mu/E_F < 0.9995$  or  $6.197 \times 10^{-5} < x < 6.604 \times 10^{-3}$  (84). The Li concentration and pair size at  $\mu = 0$  are  $x = 1.1169 \times 10^{-4}$

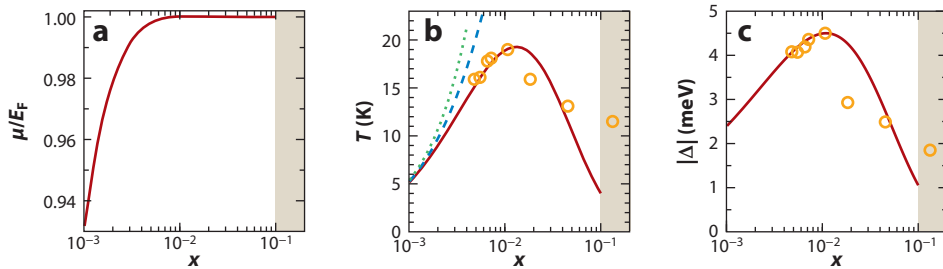


**Figure 8**

Comparison between experimental data (1) and theoretical calculations (84) for the BCS–BEC evolution in  $\text{Li}_x\text{ZrNCl}$ . (a) Chemical potential versus  $x$  at  $T = T_{\text{BKT}}$ . (b) Temperature  $T$  (in Kelvin) versus  $x$ . The dotted green line is the standard upper bound  $T_{\text{F}}/8$ , the dashed blue line is  $T_{\text{c}} = T_{\text{BKT}}$  for zero-ranged interactions, and the solid red line is  $T_{\text{c}} = T_{\text{BKT}}$  for finite-ranged interactions that produce the best fit to the experimental data in open yellow circles. (c) Modulus of the order parameter  $|\Delta|$  in millielectronvolts versus  $x$ , showing the best theoretical fit (solid red line) to the experimental data (open yellow circles). The three-dimensional regions are shown in beige; the BCS (BEC) regimes occur for higher (lower) values of  $x$ . Figure adapted with permission from Reference 84.

and  $k_{\text{F}}\xi_{\text{pair}} = 0.5969$ , respectively, whereas at the lowest experimental concentration achieved  $x_{\text{min}} = 0.0048$ ,  $k_{\text{F}}\xi_{\text{pair}} = 3.803$ , and  $\mu/E_{\text{F}} = 0.9978$ , showing that the crossover region has just been entered from the BCS side. The fact that  $T_{\text{c}}/T_{\text{F}}$  is not too far from the standard upper bound of  $1/8$  for the lowest concentrations is not a sufficient condition to demonstrate that the BEC regime has been reached. See **Figure 3a,b**, where at  $|E_{\text{b}}|/E_{\text{F}} = 0.30$ ,  $T_{\text{c}}/T_{\text{F}}$  is already very close to  $1/8$  but the chemical potential is still around  $\mu/E_{\text{F}} = 0.8506$  and, thus, is very far from  $\mu/E_{\text{F}} = 0$ . If the lowest experimental value of  $x_{\text{min}}$  can be reduced by at least one order of magnitude, then the crossover region can be explored, but reaching the BEC regime would require a reduction in  $x_{\text{min}}$  by at least two orders of magnitude.

## 6.2. Superfluids in 2D: Lack of Two-Band BCS–BEC Crossover in Ultracold Atoms

Although a few examples of experimental investigations of the crossover from BCS to BEC exist for two-band superconductors in 2D (1, 2, 7–9), analogous cases have not yet been investigated with ultracold atoms. In principle, two particle-like bands can be created for cold fermions by using a tightly confining potential along a transverse  $z$  direction, producing two kinetically confined states at different energies. The resulting parabolic dispersions along the  $xy$  plane would correspond to the situation displayed in **Figure 7a**, with the advantage that the chemical potentials  $\tilde{\mu}_1$  and  $\tilde{\mu}_2$  can be tuned independently. Thus far, only theoretical work exists covering collective modes (85), elementary excitations, phase diagrams, and critical temperature (86), which were revisited more recently (87–89). The possibility of creating two-band superfluids using optical lattices also exists, but even creating one-band Fermi superfluids in optical lattices has been difficult (90, 91).

## 7. TWO-BAND BCS–BEC IN 2D: QUANTUM PHASE TRANSITIONS

The two-band action  $S_{2\text{B}}$ , the binding energies  $E_{\text{jb}}$ , and the phase-only effective  $S_{\text{fl}}$  in Equations 7–9 can be used to investigate quantum phase transitions for the  $d$ -wave channel via the simple substitution  $\Gamma_{\mathbf{k}} = \gamma_{|\mathbf{k}|}^{2\text{D}} \cos 2\phi$ , with  $\gamma_{|\mathbf{k}|}^{2\text{D}} = (|\mathbf{k}|^2/k_1^2) / (1 + |\mathbf{k}|/k_0)^{5/2}$ . For two particle-like

parabolic bands with nodal order parameters, the BCS or BEC characteristics of the superconducting and superfluid phases are controlled by the chemical potentials of the two bands with respect to their minima:  $\tilde{\mu}_j = \mu_j - \min[\epsilon_{jk}]$ , as seen in Section 5. Each band can separately undergo a topological quantum phase transition of the Lifshitz type when each chemical potential reaches the bottom of the band, as described in Section 4. The independent control of the densities in bands 1 and 2 may be achieved in ultracold atomic fermions leading to two different chemical potentials  $\tilde{\mu}_1$  and  $\tilde{\mu}_2$ , which can be tuned to visit different phases BCS<sub>1</sub>-BCS<sub>2</sub>, BCS<sub>1</sub>-BEC<sub>2</sub>, BEC<sub>1</sub>-BCS<sub>2</sub>, and BEC<sub>1</sub>-BEC<sub>2</sub>. As discussed in Section 5, provided that the order parameters are nonzero and have a nodal structure, the structure of the phase diagram with four phases is very general, such that the phase boundaries are solely controlled by the effective chemical potentials  $\tilde{\mu}_j$  and are independent of the band masses and interaction potentials.

For superconductors with particle-like parabolic bands, only the total particle density can be fixed, so there is solely one chemical potential  $\mu$  leading to three accessible phases: BCS<sub>1</sub>-BCS<sub>2</sub> when  $\mu > \min[\epsilon_{1k}]$ ; BEC<sub>1</sub>-BCS<sub>2</sub> when  $\min[\epsilon_{2k}] < \mu < \min[\epsilon_{1k}]$ ; and BEC<sub>1</sub>-BEC<sub>2</sub> when  $\mu < \min[\epsilon_{2k}]$ . The theoretically expected topological quantum phase transitions in such systems have not yet been observed experimentally. However, in materials with particle- and hole-like bands, such as magic-angle twisted trilayer graphene (3–5), there is experimental evidence that the BCS–BEC evolution is occurring via a topological quantum phase transition from gapless to fully gapped *d*-wave superconductivity (3, 92, 93). The generic discussion encompassing Equations 7 through 9, covering two bands with particle-like dispersions, also applies to two bands with particle- and hole-like kinetic energies. Applying a particle–hole transformation to band 2, mapping  $1 \rightarrow e$  and  $2 \rightarrow b$ , and using the energy dispersions  $\epsilon_{ek} = \epsilon_{bg}/2 + \hbar^2 \mathbf{k}^2/2m_e$  and  $\epsilon_{bk} = -\epsilon_{bg}/2 - \hbar^2 \mathbf{k}^2/2m_b$  leads to the generic phase diagram shown in **Figure 9a**, where  $\tilde{\mu}_e = \mu_e - \min[\epsilon_{ek}]$  and  $\tilde{\mu}_b = \mu_b - \max[\epsilon_{bk}]$ . Using the shifted kinetic energies  $\xi_{ek} = \epsilon_{ek} - \mu_e = \hbar^2 \mathbf{k}^2/2m_e - \tilde{\mu}_e$  and  $\xi_{bk} = \epsilon_{bk} + \mu_b = -\hbar^2 \mathbf{k}^2/2m_b + \tilde{\mu}_b$  and the quasiparticle energies

$$E_{ek} = \sqrt{\xi_{ek}^2 + |\Delta_{ek}|^2} \quad \text{and} \quad E_{bk} = \sqrt{\xi_{bk}^2 + |\Delta_{bk}|^2}, \quad 11.$$

it is clear that *s*-wave pairing in both bands only leads to BCS–BEC crossovers, whereas higher angular momentum pairing with nodes (e.g., *d*-wave with  $d_{x^2-y^2}$  symmetry) may have two topological quantum phase transitions during the BCS–BEC evolution, depending on the path taken in the  $\tilde{\mu}_e$  versus  $\tilde{\mu}_b$  phase diagram shown in **Figure 9a**. For *d*-wave pairing with  $d_{x^2-y^2}$  symmetry, in analogy to the one-band case, the order parameters are  $\Delta_{jk} = |\Delta_j| \gamma_{jk}^{2D} \cos 2\phi$ .

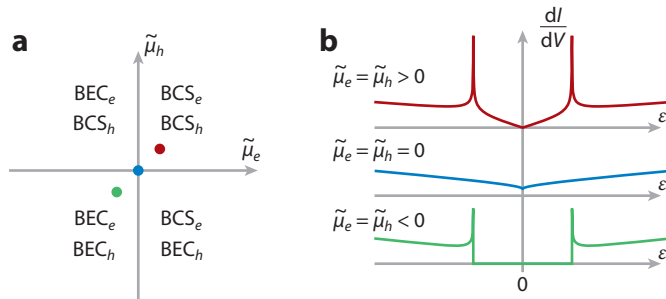


**Figure 9**

(a) Phase diagram in the  $\tilde{\mu}_b$  versus  $\tilde{\mu}_e$  plane showing superfluid or superconducting regions. (b) Qualitative plots of the  $dI/dV$  characteristics along the path of the red, blue, and green dots.

The observation of a V-shaped to U-shaped transition in the tunneling conductance ( $dI/dV$ ) data of magic-angle twisted trilayer graphene (3) and the existence of electron and hole bands in the carrier density regime explored suggests the existence of nodal order parameters and of a topological quantum phase transition analogous to those discussed above. This behavior is illustrated in **Figure 9b** for  $m_e = m_b$ , where the conditions for the order parameters  $|\Delta_{e\tilde{\mathbf{k}}_e}| \gg |\tilde{\mu}_e|$  and  $|\Delta_{b\tilde{\mathbf{k}}_b}| \gg |\tilde{\mu}_b|$ , with  $\tilde{\mathbf{k}}_{\tilde{\mu}_j}$  being the loci of  $\xi_{jk} = 0$ , produce only two peaks in the density of states  $D(\varepsilon)$  represented by the  $dI/dV$  characteristics. This observation suggests that magic-angle twisted trilayer graphene is in the low carrier density but strong-coupling regime, otherwise more peaks in the density of states would emerge (93). However, for the V-shaped to U-shaped transition observed in magic-angle twisted trilayer graphene (3), the gap never closes, as seen in **Figure 9b**, indicating that the path taken in **Figure 9a** is not accessible, as the chemical potentials  $\tilde{\mu}_e$  and  $\tilde{\mu}_b$  may not be adjusted accordingly in this system. There are four contributions to

$$D(\varepsilon) = U_{e\mathbf{k}}^2 \delta(\varepsilon - E_{e\mathbf{k}}) + V_{e\mathbf{k}}^2 \delta(\varepsilon + E_{e\mathbf{k}}) + U_{b\mathbf{k}}^2 \delta(\varepsilon - E_{b\mathbf{k}}) + V_{b\mathbf{k}}^2 \delta(\varepsilon + E_{b\mathbf{k}}), \quad 12.$$

where the first (second) two terms are due to pairing in the electron (hole) band, and  $U_{j\mathbf{k}} = \sqrt{1 + \xi_{j\mathbf{k}}/E_{j\mathbf{k}}}$  and  $V_{j\mathbf{k}} = \sqrt{1 - \xi_{j\mathbf{k}}/E_{j\mathbf{k}}}$  are the coherence factors (Bogoliubov coefficients) representing the residues of the poles at  $\varepsilon = \pm E_{j\mathbf{k}}$ , with  $j \in \{e, b\}$ . The breaking of particle-hole symmetry (e.g.,  $m_e \neq m_b$  or  $\lambda_{ee} \neq \lambda_{bb}$ ) creates asymmetries in the density of states but does not affect the topological nature of the quantum phase transition from V- to U-shaped exhibited by the  $dI/dV$  characteristics. At low carrier densities and sufficiently strong coupling, the locations of the van Hove singularities are determined by the chemical potentials  $\tilde{\mu}_e$  and  $\tilde{\mu}_b$ , resulting in two distinct peaks in the density of states. Along the paths of the dots shown in **Figure 9a** there are three distinct behaviors. At the first quadrant, the system is gapless, with  $\tilde{\mu}_e > 0$  and  $\tilde{\mu}_b > 0$ , with four Dirac points in each band, having V-shaped peaks in  $D(\varepsilon)$  at  $\varepsilon = -|\tilde{\mu}_e|$  and  $\varepsilon = +|\tilde{\mu}_b|$ . At the origin, the system is gapless with  $\tilde{\mu}_e = 0$  and  $\tilde{\mu}_b = 0$ , but the four Dirac points in each band annihilate, producing a finite  $D(\varepsilon)$  at  $\varepsilon = 0$ . At the third quadrant, the system is fully gapped, with  $\tilde{\mu}_e < 0$  and  $\tilde{\mu}_b < 0$ , without Dirac points, having U-shaped peaks in  $D(\varepsilon)$  at  $\varepsilon = +|\tilde{\mu}_e|$  and  $\varepsilon = -|\tilde{\mu}_b|$ .

For the paths taken along the dots in **Figure 9**, the topological nature of this quantum phase transition is essentially the same as visually shown in **Figure 6**. Time-reversal symmetry is not broken, but, for  $\tilde{\mu}_j > 0$ , the Dirac fermions that emerge in band  $j \in \{e, b\}$  are chiral and have winding numbers

$$N_{jw} = \frac{1}{2\pi} \oint_C d\ell \hat{\mathbf{z}} \cdot \mathbf{m}_j \times \frac{d\mathbf{m}_j}{d\ell}, \quad 13.$$

where  $\mathbf{m}_j = (\xi_{j\mathbf{k}}, \Delta_{j\mathbf{k}})/E_{j\mathbf{k}}$ , and the path  $C$  encircles each Dirac point separately. The topological index  $N_{jw}$  alternates between  $\mp 1$  ( $\phi = \pi/4, 5\pi/4$ ) and  $\pm 1$  ( $\phi = 3\pi/4, 7\pi/4$ ) as the Dirac points are circled counterclockwise, where the top (bottom) sign is for  $e$  ( $b$ ). Because there is no global chiral symmetry breaking, the net chirality of the system is zero. Nevertheless, the annihilation of chiral Dirac quasiparticles at  $\tilde{\mu}_j = 0$  defines topological quantum phase transitions in momentum space. For  $\tilde{\mu}_j < 0$ , the spectra  $E_{j\mathbf{k}}$  are fully gapped, with  $\min[E_{j\mathbf{k}}] = |\tilde{\mu}_j|$  at  $|\mathbf{k}| = 0$ , and  $N_{jw}$  is always zero everywhere in momentum space, because chiral Dirac quasiparticles no longer exist.

Similar to the one-band case, a thermodynamic signature of the topological quantum phase transitions also arises in the isothermal compressibility  $n^2 \kappa_T = \partial n / \partial \mu|_{T,V}$ . For a system with two parabolic bands and nodal  $d$ -wave order parameters, logarithmic singularities arise in  $\kappa_T$  each time

a topological phase boundary is crossed (93). For example, in the case of one-particle and one-hole parabolic bands,  $\kappa_T \approx -\alpha_c \ln |\tilde{\mu}_c|/E_0 + \beta_c$  near  $\tilde{\mu}_c = 0$  or  $\kappa_T \approx -\alpha_b \ln |\tilde{\mu}_b|/E_0 + \beta_b$  near  $\tilde{\mu}_b = 0$ . The coefficient  $\alpha_j$  ( $\beta_j$ ) is independent of (dependent on) the sign of  $\tilde{\mu}_j$ . For order parameters with nodal  $p$ -wave symmetry (e.g.,  $p_x$  or  $p_y$ ), the transition is less dramatic:  $\kappa_T$  displays a cusp when  $\tilde{\mu}_j = 0$ , meaning that its derivatives are not continuous (48, 79).

## 8. SUMMARY

We have reviewed a few conceptual ideas regarding the evolution from BCS to BEC superfluidity and superconductivity in 2D. We discussed one-band and two-band continuum and lattice systems, where crossovers and topological quantum phase transitions can occur as the chemical potentials are changed. We emphasized the role played by chemical potentials in creating BCS- or BEC-like phases. We remarked that in practice the tuning of chemical potentials can be achieved by changing either carrier density at fixed interactions for superconductors or interactions at fixed particle density for ultracold Fermi superfluids. We highlighted that nonnodal  $s$ -wave pairing always leads to crossovers, whereas higher angular momentum nodal pairing, such as  $d$ -wave, leads to topological quantum phase transitions from gapless to fully gapped superconductors and superfluids. We also reviewed connections between theory and experiments for one-band ultracold Fermi superfluids such as  ${}^6\text{Li}$  and for two-band superconductors such as  $\text{Li}_x\text{ZrNCl}$  and magic-angle twisted trilayer graphene, where the BCS–BEC evolution has been explored.

## 9. OUTLOOK

Most of this review covered BCS–BEC evolutions in 2D for one- and two-band superconductors or superfluids with parabolic bands. However, there are several open problems that require theoretical attention, three of which are listed below.

An important open question is the development of a microscopic theory, beyond phase fluctuations, that can recover the Fisher–Hohenberg logarithmic corrections to the critical temperature  $T_c$  of two-dimensional superconductors and superfluids when the binding energy is very strong. Fluctuations in the modulus of the order parameter, beyond Gaussian order, are necessary to recover the boson–boson interactions responsible for the Fisher–Hohenberg corrections. The development of such a microscopic theory is crucial for comparisons to experiments deep into the BEC regime.

Another important issue is the existence of tight bounds on  $T_c$  of two-dimensional superconductors and superfluids. The standard upper bound for  $T_c$  in one-band systems, based on the bare superfluid density, is always limited by the kinetic energy and thus is independent of interactions and of the symmetry of the order parameter, either in the continuum (32) or in the lattice (94). However, this upper bound is not generally tight (95), and thus not very useful. For one-band systems, tighter upper bounds from the renormalized superfluid density exist (96), but attempts to use the standard bound for multiband superconductors (94) have been criticized (97). This leaves the question of the existence of tight upper bounds on  $T_c$  for two-band superconductors and superfluids wide open.

The evolution from BCS to BEC in one-band lattices has been theoretically explored with ultracold atoms, and topological quantum phase transitions have been identified (49) but not yet experimentally observed (80). However, as illustrated in **Figure 10**, two-band systems offer a new degree of complexity and richness of phases, as well as the possibility of connecting to experiments in multiband superconductors like  $\text{FeSe}$  and  $\text{FeSe}_{1-x}\text{S}_x$ , where lattice effects may be important (6–9).

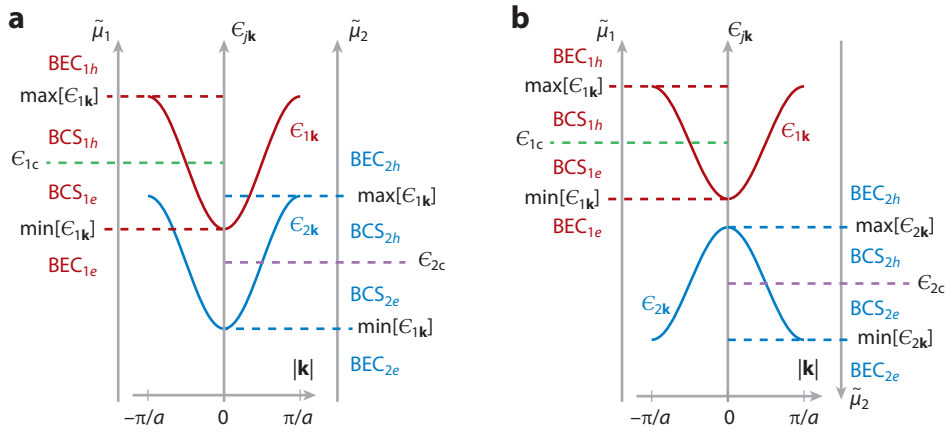


**Figure 10**

Phase diagrams for chemical potentials  $\tilde{\mu}_1$  and  $\tilde{\mu}_2$  and sketches of energy dispersions for lattices with two particle-like bands are shown in panel *a* and for lattices with one particle-like and one hole-like bands are shown in panel *b*.

## DISCLOSURE STATEMENT

The authors are not aware of any affiliations, memberships, funding, or financial holdings that might be perceived as affecting the objectivity of this review.

## ACKNOWLEDGMENTS

We acknowledge the support of the Belgian American Educational Foundation.

## LITERATURE CITED

- Nakagawa Y, Kasahara Y, Nomoto T, Arita R, Nojima T, Iwasa Y. 2021. *Science* 372:190–95
- Heyl M, Adachi K, Itahashi YM, Nakagawa Y, Kasahara Y, et al. 2022. *Nat. Commun.* 13:6986
- Kim H, Choi Y, Lewandowski C, Thomson A, Zhang Y, et al. 2022. *Nature* 606(7914):494–500
- Park JM, Cao Y, Watanabe K, Taniguchi T, Jarillo-Herrero P. 2021. *Nature* 590:249–55
- Hao Z, Zimmerman AM, Ledwith P, Khalaf E, Najafabai DH, et al. 2021. *Science* 371(6534):1133–38
- Kasahara S, Watashige T, Hanaguri T, Kohsaka Y, Yamashita T, et al. 2014. *PNAS* 111(46):16309–13
- Hanaguri T, Kasahara S, Böker J, Eremin I, Shibauchi T, Matsuda Y. 2019. *Phys. Rev. Lett.* 122:077001
- Hashimoto T, Ota Y, Tsuzuki A, Nagashima T, Fukushima A, et al. 2020. *Sci. Adv.* 6:eabb9052
- Mizukami Y, Haze M, Tanaka O, Matsuura K, Sano D, et al. 2023. *Commun. Phys.* 6:183
- Sobirey L, Luick N, Bohlen M, Biss H, Moritz H, Lompe T. 2021. *Science* 372(6544):844–46
- Sobirey L, Biss H, Luick N, Bohlen M, Moritz H, Lompe T. 2022. *Phys. Rev. Lett.* 129(8):083601
- Bardeen J, Cooper LN, Schrieffer JR. 1957. *Phys. Rev.* 108(5):1175–204
- Schafroth MR, Butler ST, Blatt JM. 1957. *Helv. Phys. Acta* 30:93–134
- Blatt JM. 1964. *Theory of Superconductivity*. New York: Academic
- Leggett AJ. 1980. In *Modern Trends in the Theory of Condensed Matter, Proc. XVI Karpacz Winter School of Theoretical Physics*, ed. A Pekalski, JA Przystawa, pp. 13–27. Berlin: Springer-Verlag
- Leggett AJ. 1980. *J. Phys. Colloq.* 41(C7):19–26
- Nozières P, Schmitt-Rink S. 1985. *J. Low Temp. Phys.* 59(3):195–211
- Sá de Melo CAR, Randeria M, Engelbrecht JR. 1993. *Phys. Rev. Lett.* 71(19):3202–5
- Engelbrecht JR, Randeria M, Sá de Melo CAR. 1997. *Phys. Rev. B* 55(22):15153–56
- Zwierlein MW, Stan CA, Schunck CH, Raupach SMF, Gupta S, et al. 2003. *Phys. Rev. Lett.* 91(25):250401
- Jochim S, Bartenstein M, Altmeyer A, Hendl G, Riedl S, et al. 2003. *Science* 302(5653):2101–3

22. Strecker KE, Partridge GB, Hulet RG. 2003. *Phys. Rev. Lett.* 91(8):080406
23. Kinast J, Hemmer SL, Gehm ME, Turlapov A, Thomas JE. 2004. *Phys. Rev. Lett.* 92:150402
24. Bourdel T, Khaykovich L, Cubizolles J, Zhang J, Chevy F, et al. 2004. *Phys. Rev. Lett.* 93:050401
25. Zwierlein MW, Abo-Shaer JR, Schirotzek A, Schunck CH, Ketterle W. 2005. *Nature* 435(7045):1047–51
26. Greiner M, Regal CA, Jin DS. 2003. *Nature* 426(6966):537–40
27. Regal CA, Greiner M, Jin DS. 2004. *Phys. Rev. Lett.* 92(4):040403
28. Feshbach H. 1958. *Ann. Phys.* 5(4):357–90
29. Fano U. 1961. *Phys. Rev.* 124(6):1866–78
30. Regal CA, Ticknor C, Bohn JL, Jin DS. 2003. *Phys. Rev. Lett.* 90(5):053201
31. Gaebler JP, Stewart JT, Bohn JL, Jin DS. 2007. *Phys. Rev. Lett.* 98(20):200403
32. Botelho SS, Sá de Melo CAR. 2006. *Phys. Rev. Lett.* 96:040404
33. Feld M, Fröhlich B, Vogt E, Koschorreck M, Köhl M. 2011. *Nature* 480:75–78
34. Bertaina G, Giorgini S. 2011. *Phys. Rev. Lett.* 106:110403
35. Fenech K, Dyke P, Peppler T, Lingham M, Hoinka S, et al. 2016. *Phys. Rev. Lett.* 116:045302
36. Iskin M, Sá de Melo CAR. 2009. *Phys. Rev. Lett.* 103:165301
37. Dyke P, Kuhnle ED, Whitlock S, Hu H, Mark M, et al. 2011. *Phys. Rev. Lett.* 106:105304
38. Sommer AT, Cheuk LW, Ku MJH, Bakr WS, Zwierlein MW. 2011. *Phys. Rev. Lett.* 108:045302
39. Ries M, Wenz A, Zürn G, Bayha L, Boettcher I, et al. 2011. *Phys. Rev. Lett.* 114:230401
40. Boettcher I, Bayha L, Kedar D, Murthy P, Neidig M, et al. 2011. *Phys. Rev. Lett.* 116:045303
41. Baksmaty LO, Lu H, Bolech CJ, Pu H. 2011. *New J. Phys.* 13:055014
42. Imambekov A, Bolech CJ, Lukin M, Demler E. 2006. *Phys. Rev. A* 74:053626
43. Mukherjee B, Yan Z, Patel PB, Hadzibabic Z, Yefsah T, et al. 2017. *Phys. Rev. Lett.* 118(12):123401
44. Hueck K, Luick N, Sobirey L, Siegl J, Lompe T, Moritz H. 2018. *Phys. Rev. Lett.* 120(6):060402
45. Baird L, Wang X, Roof S, Thomas JE. 2019. *Phys. Rev. Lett.* 123(16):160402
46. Navon N, Smith RP, Hadzibabic Z. 2021. *Nat. Phys.* 17:1334–41
47. Schumacher GL, Mäkinen JT, Ji Y, Assumpção GG, Chen J, et al. 2023. arxiv:2301.02237
48. Botelho SS, Sá de Melo CAR. 2005. *Phys. Rev. B* 71:134507
49. Iskin M, Sá de Melo CAR. 2005. *Phys. Rev. B* 72(22):224513
50. Petrov DS, Baranov MA, Shlyapnikov GV. 2003. *Phys. Rev. A* 67:031601(R)
51. Bohlen M, Sobirey L, Luick N, Biss H, Enss T, et al. 2020. *Phys. Rev. Lett.* 124(24):240403
52. Sá de Melo CAR. 2008. *Phys. Today* 61(10):45–51
53. Duncan RD, Sá de Melo CAR. 2000. *Phys. Rev. B* 62(14):9675
54. Deleted in proof
55. Borkowski LS, Sá de Melo CAR. 2001. *Acta Phys. Pol.* 99(6):691–98
56. Botelho SS. 2005. *BCS-to-BEC quantum phase transition in high-Tc superconductors and fermionic atomic gases: A functional integral approach*. PhD Thesis, Georgia Institute of Technology, Atlanta
57. Petrov DS, Shlyapnikov GV. 2001. *Phys. Rev. A* 64:012706
58. Berezinskii V. 1971. *Sov. Phys. JETP* 32(3):493–500
59. Kosterlitz JM, Thouless DJ. 1972. *J. Phys. C: Solid State Phys.* 5(11):L124–26
60. Nelson DR, Kosterlitz JM. 1977. *Phys. Rev. Lett.* 39(19):1201–5
61. Devreese JPA, Tempere J, Sá de Melo CAR. 2014. *Phys. Rev. Lett.* 113(16):165304
62. Devreese JPA, Tempere J, Sá de Melo CAR. 2015. *Phys. Rev. A* 92(4):043618
63. Fisher DS, Hohenberg PC. 1988. *Phys. Rev. B* 37(10):4936–43
64. Perali A, Pieri P, Strinati GC. 2004. *Phys. Rev. Lett.* 93(10):100404
65. Bulgac A. 2007. *Phys. Rev. A* 76:040502(R)
66. Zwierlein MW, Schunck CH, Schirotzek A, Ketterle W. 2006. *Nature* 442:54–58
67. Zhou Q, Ho TL. 2011. *Phys. Rev. Lett.* 106:225301
68. Köhl M. 2022. Machine Learning Based Detection of Phase Transitions. <https://www.pi.uni-bonn.de/koehl/en/research/humphry>
69. Combescot R, Kagan MY, Stringari S. 2006. *Phys. Rev. A* 74(4):042717
70. Kurkjian H, Castin Y, Sinatra A. 2016. *Phys. Rev. A* 93:013623
71. Van Loon S, Sá de Melo CAR. 2023. *Phys. Rev. Lett.* 131:113001

72. Lifshitz IM. 1960. *Sov. Phys. JETP* 11:1130–35
73. Randeria M, Duan J, Shien L. 1990. *Phys. Rev. B* 41(19):327–43
74. Read N, Green D. 2000. *Phys. Rev. B* 61:10267
75. Cao G, He L, Huang XG. 2017. *Phys. Rev. A* 96(6):063618
76. Harrison N, Chan MK. 2022. *Phys. Rev. Lett.* 129:017001
77. Sous J, He Y, Kivelson SA. 2023. *npj Quantum Mater.* 8:25
78. Kayyalha M, Xiao D, Zhang R, Shin J, Jiang J, et al. 2020. *Science* 367(6473):64–67
79. Botelho SS, Sá de Melo CAR. 2004. arxiv:cond-mat/0409357
80. Venu V, Xu P, Mamaev M, Corapi F, Bilitewski T, et al. 2023. *Nature* 613(7943):262–67
81. Zwierlein MW, Schirotzek A, Schunck CH, Ketterle W. 2006. *Science* 311(5760):492–96
82. Liao Ya, Rittner ASC, Paprotta T, Li W, Partridge GB, et al. 2006. *Science* 311(5760):492–96
83. Sá de Melo CAR. 2014. In *Multi-Condensates Superconductivity (Erice Lectures)*. Rome: Superstripes. (Abstr.)
84. Shi T, Zhang W, Sá de Melo CAR. 2022. *EPL* 139:36003
85. Iskin M, Sá de Melo CAR. 2005. *Phys. Rev. B* 72:024512
86. Iskin M, Sá de Melo CAR. 2006. *Phys. Rev. B* 74:144517
87. Tajima H, Yerin Y, Perali A, Pieri P. 2019. *Phys. Rev. B* 99(18):180503
88. Yerin Y, Tajima H, Pieri P, Perali A. 2019. *Phys. Rev. B* 100:104528
89. Shi YR, Zhang W, Sá de Melo CAR. 2022. *EPL* 139:36004
90. Köhl M, Moritz H, Stöferle T, Günther K, Esslinger T. 2005. *Phys. Rev. Lett.* 94:080403
91. Chin J, Miller D, Liu Y, Stan C, Setiawan W, et al. 2006. *Nature* 443:961–64
92. Lewandowski C, Lantagne-Hurtubise E, Thomson A, Nadj-Perge S, Alicea J. 2022. *Phys. Rev. B* 107:L020502
93. Van Loon S, Sá de Melo CAR. 2023. arxiv:2303.05017
94. Hazra T, Verma N, Randeria M. 2019. *Phys. Rev. X* 9:031049
95. Shi T, Zhang W, Sá de Melo CAR. 2022. arxiv:2203.05478
96. Shi T, Zhang W, Sá de Melo CAR. 2023. arxiv:2303.10939
97. Hofmann JS, Chowdhury D, Kivelson SA, Berg E. 2022. *NPJ Quantum Mater.* 7:83